View Article Online
DOI: 10.1039/D2TB01352E

Antibacterial nanopatterned coatings for dental implants

Raul Fontelo[a,b], Diana Soares da Costa[a,b], Manuel Gomez-Florit[a,b†], Hanna Tiainen[c], Rui L. Reis[a,b], Ramon Novoa-Carballal[,a,b], Iva Pashkuleva[*,a,b]*

[a] 3B's Research Group, I3Bs – Research Institute on Biomaterials, Biodegradables and Biomimetics, University of Minho, Headquarters of the European Institute of Excellence on Tissue Engineering and Regenerative Medicine, AvePark, Parque de Ciência e Tecnologia, Zona Industrial da Gandra, 4805-017 Barco, Portugal;

[b] ICVS/3B's–PT Government Associate Laboratory, Braga/Guimarães, Portugal.

[c] Department of Biomaterials, Institute of Clinical Dentistry, University of Oslo, P.O. box 1109, Blindern, Oslo 0317, Norway

[†] Present address: Health Research Institute of the Balearic Islands (IdISBa), 07010 Palma, Spain.

Abstract

Dental implants, usually made of titanium, are exposed to hostile oral microflora that facilitates bacterial infections and subsequent inflammation. To mitigate these processes, we coated titanium substrates with block copolymer nanopatterns and investigated the bactericidal effect of these coatings against gram-positive and gram-negative bacteria. We found that the bactericidal efficacy of the coatings depends on their morphology and surface chemistry as well as on the bacterial strain: an optimal combination can lead to significant bacterial death for a short time, i.e. 90 % for 90 min. Human gingival fibroblasts in contact with the nanopatterned coatings showed similar cell attachment and morphology as on bare Ti. Immunostaining assays showed similar levels of CCR7 and CD206 in macrophages cultured over the nanopatterns and bare Ti, demonstrating adequate properties for tissue integration. The nanopatterns induced a small increase in macrophage aspect ratio, which might indicate early states of M2 polarization, given the absence of CD206.

Introduction

View Article Online
DOI: 10.1039/D2TB01352E

Dental implants are a common clinical choice for the management of tooth loss. Among different alternatives, implants made of titanium or titanium alloys are the most used due to their biocompatibility and mechanical properties.[1,2] Although the success rate of dental implants is relatively high, the clinical outcome might be compromised due to a lack of osteointegration or implant-related infections that ultimately cause implant failure.[3] For example, the prevalence of peri-implant mucositis and peri-implantitis is around 30% and 10-30%, respectively, 5 to 10 years after the implantation.[4-6] The infection is usually related to loose contact between the device and the soft tissue leading to bacterial penetration around the implant or chronic gingival inflammation.[7] The surface properties of the implant, such as chemistry and roughness, play a decisive role in both processes.[8] Thus, different surface modifications have been proposed to render the implant with antibacterial properties. These approaches can be generally classified in three groups: antibiotic(s)-releasing coatings, anti-biofouling surfaces, and surfaces with contact-killing capacity.[9, 10] Each of these approaches has advantages and drawbacks. For example, several disadvantages have been reported for the antibiotic(s)-releasing coatings: they can be cytotoxic and cause inflammation or bacterial resistance.[11, 12] The anti-biofouling approaches also have some disadvantages - they hamper cell attachment and hence tissue integration.[13] Bactericidal bio-mimicking nanostructures have emerged as an alternative approach: such contact-killing surfaces act by mechanical disruption of the bacterial wall.[14, 15] Besides their contact-killing capacity, these nanostructures have the advantage of enhancing the adhesion between the implant and the soft tissue, thus reducing the risk of infection.[16] However, fabrication of such nanostructured coatings is challenging, usually costly and requires specific equipment.[17] Herein, we propose self-assembly of the block copolymer (BCP) poly(styrene-*block*-2-vinylpyridine), abbreviated as PS-*b*-P2VP, on titanium as a way to reduce implant-related infections and enhance implant integration. This approach is simple (Fig. 1), cost-effective, does not require dedicated equipment, and allows coating of large surface areas with precise control of the nanotopography by changing the molecular weight of the block or the processing conditions (solvent, temperature, humidity).[18] We have demonstrated its feasibility for the development of bactericidal (contact-killing) and biocompatible surfaces in a recent proof of concept study.[19] Similar coatings, i.e. vertical parallel cylinders assembled from another BCP, namely

View Article Online
DOI: 10.1039/D1TB01352E

poly(styrene-*block*-poly(methyl methacrylate) PS-*b*-PMMA have an antifouling affect on *E. coli* and *S. aureus*.[20] Moreover, bioactive molecules can be incorporated in such nanopatterns to add the antibacterial properties: PS-*b*-P4VP functionalized with antibacterial silver nanoparticles and C_{70} (fullerene, known for its virucidal effect) showed enhanced antibacterial properties.[21] On the other hand, BCP self-assembly has also been explored to develop cytocompatible nanopatterns with osteogenic properties.[22-25] These previous studies are very promising, but the used substrates (silicon wafers or glass)[26-28] are not appropriate for biomedical applications. Change of the substrate implies different interactions between BCP and the material surface, which can alter the nanocoating structure.[29] Thus, this study aims to validate the formation of bactericidal nanopatterns by BCP self-assembly on titanium, that is the gold standard material for bone and dental implants. The bactericidal performance of the coatings was evaluated using gram-positive and gram-negative bacterial strains. Moreover, the response of gingival fibroblasts and macrophages to the surfaces was also analyzed.

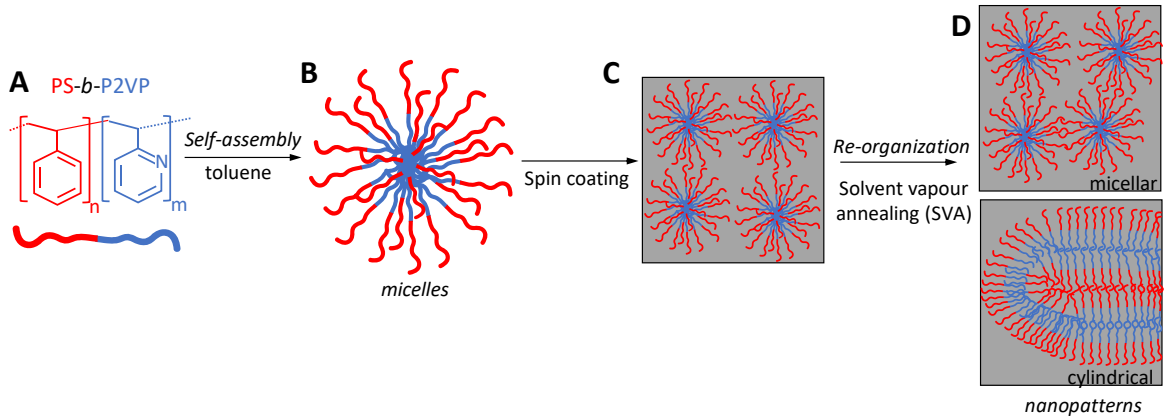

Figure 1. Schematic presentation of (A) chemical structure of the block copolymer used in this study and (B-D) different steps in the nanopatterns elaboration: (B) the polymer is dissolved in toluene where it forms micelles; (C) the solution is casted (spin coating) on Ti substrates; (D) the coated substrates are exposed to a saturated atmosphere of organic solvent (toluene or chloroform) to obtain the final nanopatterns.

Materials and Methods

Materials

View Article Online
DOI: 10.1039/D1TB01352E

Grade IV coin-shaped titanium (Ti) samples (6.2 mm diameter and 2.0 mm height) were mirror-polished and washed as previously described.[30] The coins were stored in 70 % ethanol at room temperature until further use. Poly(styrene-*block*-2-vinylpyridine) PS-*b*-P2VP with a molecular weight of the blocks M_n (PS) = 320,000 g/mol and M_n (P2VP) = 398,000 g/mol and a polydispersity index M_w/M_n = 1.10 were purchased from Polymer Source Inc. Toluene and chloroform were purchased from Fisher Chemical. Phosphate buffer saline (PBS), α-MEM medium, and phorbol-12-myristate 13-acetate (PMA) were purchased from Sigma-Aldrich. RPMI 1640 Medium, GlutaMAX™ Supplement, HEPES, antibiotic-antimycotic (streptomycin and penicillin), and fetal bovine serum (FBS) were purchased from Gibco.

Titanium coating and characterization

PS-*b*-P2VP (Fig. 1A) was dissolved in toluene at 1 wt% or 1.5 wt% overnight at room temperature and then filtered (0.22 µm PTFE). Before use, the Ti substrates were exposed to UV using a UV/Ozone cleaner (ProCleaner, Bioforce) for 15 min. The cleaned substrates were spin-coated (Fig. 1C) in a cleanroom environment at 2000 rpm for 40 s. Then the samples were exposed to a saturated atmosphere of toluene or chloroform (solvent vapor annealing, SVA, Fig. 1D) for 3 h, as described before.[19] The coated substrates were dried at room temperature and purged with a nitrogen to remove any residual solvent. The assembled nanopatterns were characterized in air by atomic force microscopy (AFM, DIMENSION icon, BRUKER) using silicon nitride cantilevers (spring constant of 0.4 N/m and frequency of 70 kHz) and PeakForce Tapping (ScanAsyst). Size and roughness of the patterns were calculated from 4 different images with the AFM software NanoScope Analysis 1.5.

Bacterial culture and analysis

Gram-negative, *Escherichia coli* (*E. coli*, ATCC 25922), and gram-positive *Staphylococcus aureus* (*S. aureus*, ATCC 25923) fresh cultures were inoculated in Luria-Bertani broth at 37 °C (150 rpm) for overnight growth. Overnight cultures were diluted in PBS until a final concentration of 2×10^8 bacteria/mL. Coated and uncoated (control) Ti substrates were incubated in the respective bacteria suspension for 30 and 90 min at 37 °C. After incubation, the samples were gently washed with PBS, stained with the Live/Dead kit BacLight (Invitrogen) following the manufacturer protocol, and observed immediately after the staining under a fluorescence microscope (Inverted Microscope Axio Observer, Zeiss). Images were processed

View Article Online
DOI: 10.1039/D2TB01352E

with Fiji (Image J) for live and dead bacteria quantification. The size of the region of interest (ROI) was set to 1399x1040 pixels (710 x 532 μm^2) and 2-3 images for each condition were analyzed. The presented data were obtained from three independent experiments with duplicates in each experiment. Morphological changes were observed by scanning electron microscopy (SEM). After each time point, substrates were fixed with 2.5 % glutaraldehyde in PBS for 1 h at 4 °C. Fixed samples were dehydrated in graded series of ethanol solutions, dried, coated with platinum (1 nm) and observed by high-resolution scanning electron microscopy (HRSEM, Auriga Compact, ZEISS) at 5kV.

Human Gingival Fibroblast culture

Primary human gingival fibroblasts (Provitro AG, HGF) from passages 3 to 6 were used. Coated and uncoated (control) Ti substrates were sterilized with UV for 30 min and washed with sterile PBS. HGF (950 cells/cm^2) were cultured on the substrates in α-MEM supplemented with 10 % FBS and 1 % antibiotic/antimycotic solution. Cultures were maintained at 37 °C and 5 % CO_2 for 30 min, 90 min, and 24 h for a preliminary cytotoxicity evaluation. After this time, the media was aspirated, and substrates were washed with PBS, fixed with 10 % buffered formalin at 4 °C for 1 h. To explore cell adhesion, cell nucleus and actin were stained with DAPI (1:500) and phalloidin-TRITC (1:200), respectively. The stained samples were mounted on microscopy slides with Vectashield (Vector Labs). Tile images of the whole sample were taken with a fluorescence microscope (Inverted Microscope Axio Observer). Cell count was performed on DAPI stained samples with Fiji (Image J) using the particle analyzer. The size of the ROI was 6578x6652 pixels (6730 x 6810 μm^2). The presented data were obtained from three independent experiments with duplicates of each condition.

Macrophages polarization assay

THP-1 cells (ECACC 88081201) were cultured in RPMI 1640 Medium, with GlutaMAX™ and HEPES, supplemented with 10% FBS and 1% antibiotic/antimycotic solution at 37 °C and 5% CO_2. Macrophage differentiation was performed in 35 mm UPcell culture plates (ThermoFisher Scientific) at a density of 1 x 10^6 cells/plate and stimulated with 100 nM phorbol-12-myristate 13-acetate (PMA) for 24 h. Cells were washed with fresh media (37 °C) and cultured for another 48 h. Afterward, adhered M0 macrophages were detached according to UPcell plate

View Article Online
DOI: 10.1039/D1TB01352E

manufacturer indications and cultured on the substrates (bare Ti used as a control and coated Ti substrates) at a density of 9.5 x 10^4 cells/cm^2 using complete culture media. To evaluate the polarization toward M1 or M2-like phenotypes, the specific markers, CCR7 and CD206, were used. After 24 h of culture, the surfaces were washed with PBS and fixed with 10 % buffered formalin. The samples were stained with primary antibody anti-CCR7 (1:250, rabbit IgG, abcam, UK) or anti-CD206 (1:50, mouse IgGS, SantaCruz Biotechnology) and secondary antibodies, donkey anti-rabbit IgG Alexa Fluor 488 (1:200; ThermoFisher Scientific) and rabbit anti-mouse IgG Alexa Fluor 488 (1:200; ThermoFisher Scientific), respectively. Nuclei and cytoskeleton were stained using DAPI and Phalloidin-TRITC, as previously described. Samples were visualized using an inverted fluorescence microscope (Axio Observer, Zeiss). The cell aspect ratio was calculated from the tile images acquired for each sample. The quantification was performed with the particle analysis tool of Fiji (Image J) using the aspect ratio subset and after establishing a threshold. CCR7 expression was quantified by applying a threshold to discard background pixels, and then the area of green pixels, corresponding to CCR7 positively stained cells, was divided by the number of cells. The experiments were repeated three times with duplicates of each condition.

Statistical Analysis

Statistical analysis was performed using the software GraphPad Prism 9. The normality of the data was evaluated using a Shapiro-Wilk test ($p < 0.05$). One-way ANOVA was applied to analyze the differences between groups with a Tukey test for post hoc analysis. Statistical significance was defined at $p < 0.05$, $p < 0.01$, $p < 0.001$, $p < 0.0001$. Data are presented as mean ± standard deviation from three independent experiments.

Results and discussion

Nanopatterns preparation over titanium

In our previous study, we generated nanopatterns with different topography by BCP self-assembly of PS_{320}-*b*-$P2VP_{380}$ on glass substrates.[19] Because of the promising bactericidal effect that these patterns showed, we have used the same BCP for this study. Applying the processing parameters established for the glass coatings (spin rate 3000 rpm, 1% and 1.5% wt

View Article Online
DOI: 10.1039/D1TB01352E

concentration, and 40 μL volume of polymer solution), we were not able to generate uniform coatings on Ti. The Ti substrates have a rougher surface (Fig. S1), and smaller dimensions than the previously used glass substrates. As a result, the coatings deposited and these conditions were discrete because the BCP solution could not penetrate in the surface microcavities. Thus, the concentration, volume and spin rate were steeply decreased until the solution was distributed uniformly in the whole surface (1% wt, 2000 rpm and 20 μL). The coated substrates (Fig. 2A) were exposed to a saturated atmosphere of either toluene or chloroform. This process is known as solvent vapor annealing (SVA) and allows molecular reorganization of the coating (Fig. 1) that depends on the blocks' solubility and the molecular mobility in the used solvent. When toluene was used (a good solvent for PS), we obtained micellar structures (Fig. 2A) while the use of chloroform (good solvent for both PS and P2VP) resulted in assembly of cylindrical features (Fig. 2B).

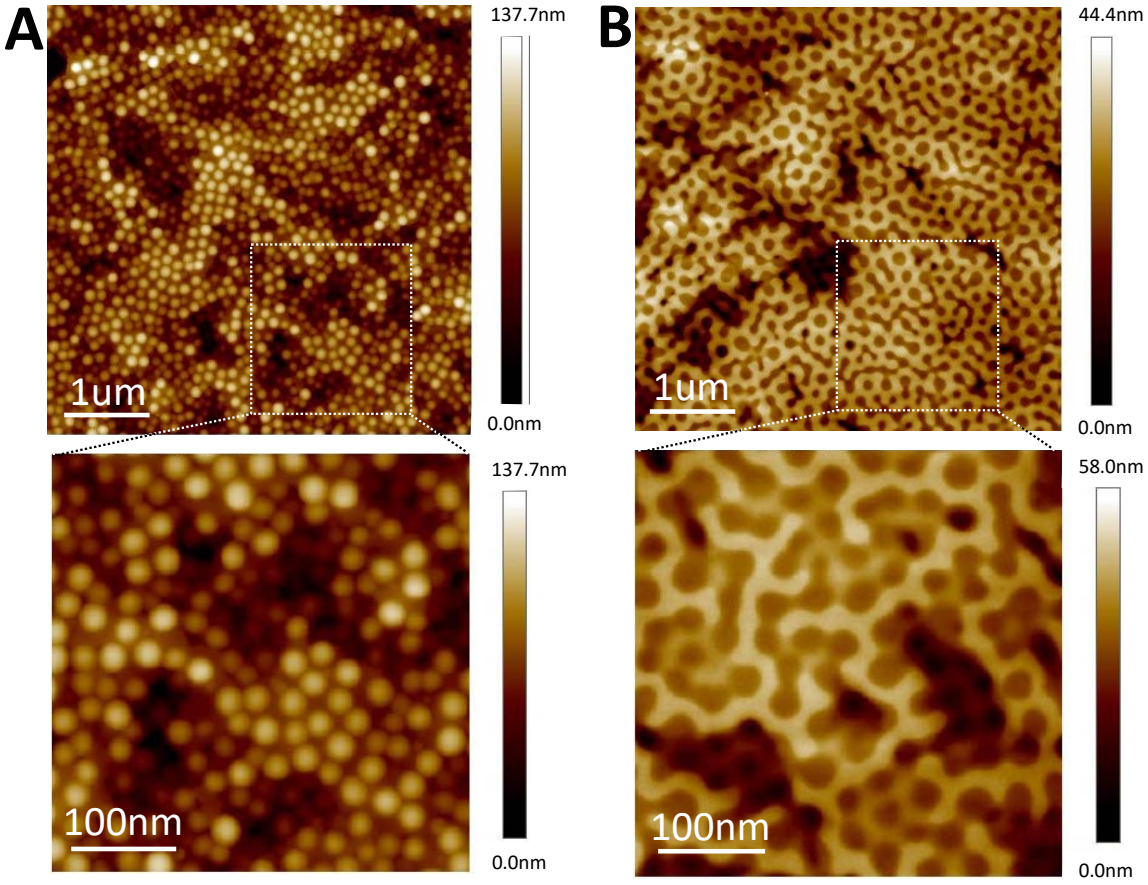

Figure 2. Representative atomic force microscopy (AFM) images of (A) micellar nanopattern assembled after solvent vapor annealing (SVA) in toluene; and (B) cylindrical nanopattern generated by SVA in chloroform.

View Article Online
DOI: 10.1039/D1TB01352E

Besides different surface morphology, the SVA process also results in patterns with different surface chemistry - the micellar nanopatterns assembled in toluene have PS exposed on the surface and a P2VP inner core (Fig. 1A), while the cylindrical nanopatterns formed by SVA in chloroform have both blocks exposed on the surface because of their excellent solubility on this solvent.[31] The topographical analysis showed a roughness of ~10 nm for the micellar nanopatterns and ~5 nm for the cylindrical ones (Table 1).

Table 1. Quantitative morphological characterization of the nanopatterns by atomic force microscopy. The PS and P2VP blocks were distinguished by staining with gold salt ($AuCl_4$).

Nanopattern	PS size (nm)[a]	P2VP size (nm)[a]	Ra (nm)
Micellar	107.27±18.53 39.78±14.35 (intermicellar)	--	10.10±2.96
Cylindrical	83.39±17.28	125.55±18.12	5.58±1.17

[a] Size in the micellar patterns corresponds to the mean micelle diameter and the distance between micelles. In the case of a cylindrical pattern, it corresponds to the mean width of the PS or PV2P.

Bactericidal properties

Dental implants are exposed to a hostile bacterial environment in the oral cavity from the very beginning of their application – bacterial colonization occurs 30 min after the implant placement.[32] The following formation of biofilm serves as a source of pathogens for peri-implantitis and depends on the surface properties of the implant.[33] To investigate the bactericidal properties of the developed patterns, we used two bacterial strains - *Escherichia coli* (*E. coli*) as a model for gram-negative bacteria, and *Staphylococcus aureus* (*S. aureus)* as representative gram-positive bacteria. After 30 min, the bacterial survival of gram-negative bacteria was reduced by either of the nanopatters (Fig. 3A). On the other hand, only the cylindrical nanopattern was effective against gram-positive bacteria at this short time of culture (Fig. 4A). This trend was maintained for a longer culture time (90 min, Figs. 3D,F and 4D,F), when a remarkable bactericidal effect was observed in the case of *E. coli* (a survival rate

View Article Online
DOI: 10.1039/D2TB01352E

of only 13 %, Fig. 3D,F) and prominent cell death was visible for *S. aureus* (survival rate of 47 %, Fig. 4D,F).

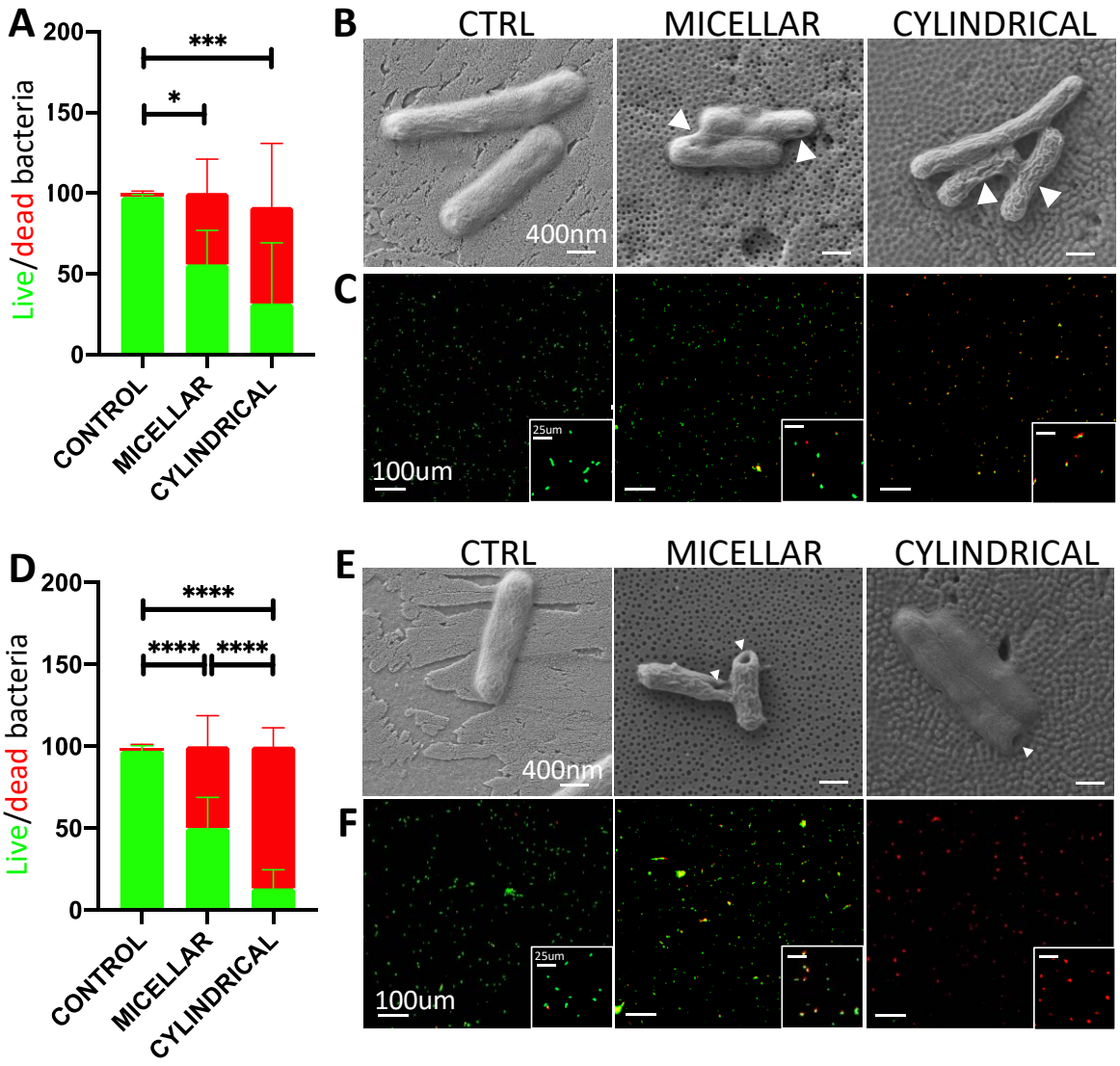

Figure 3. Bactericidal effect of the nanopatterns on gram negative bacteria (*E. coli*) observed after (A-C) 30 and (D-F) 90 min: (A, D) quantitative data obtained by live/dead assay; (B, E) representative SEM images of the bacteria on the nanopatterns (white arrows show damaged bacteria); and (C-F) representative fluorescence microscopy images of bacteria on different patterns after live dead assay (live bacteria are stained in green and dead ones in yellow/red [34]). Bare titanium was used as a control (CTRL). Statistical differences: *$p < 0.05$ ***$p < 0.001$, ****$p < 0.0001$.

View Article Online
DOI: 10.1039/D1TB01352E

A closer look at the bacteria in contact with the nanopatterns revealed damaged *E. coli* walls (Fig. 3B,E) and cell shrinking, which were previously associated with the leakage of cytoplasmic constituents.[35] Such morphological changes were not visible for *S. aureus* (Fig. 4B,E).

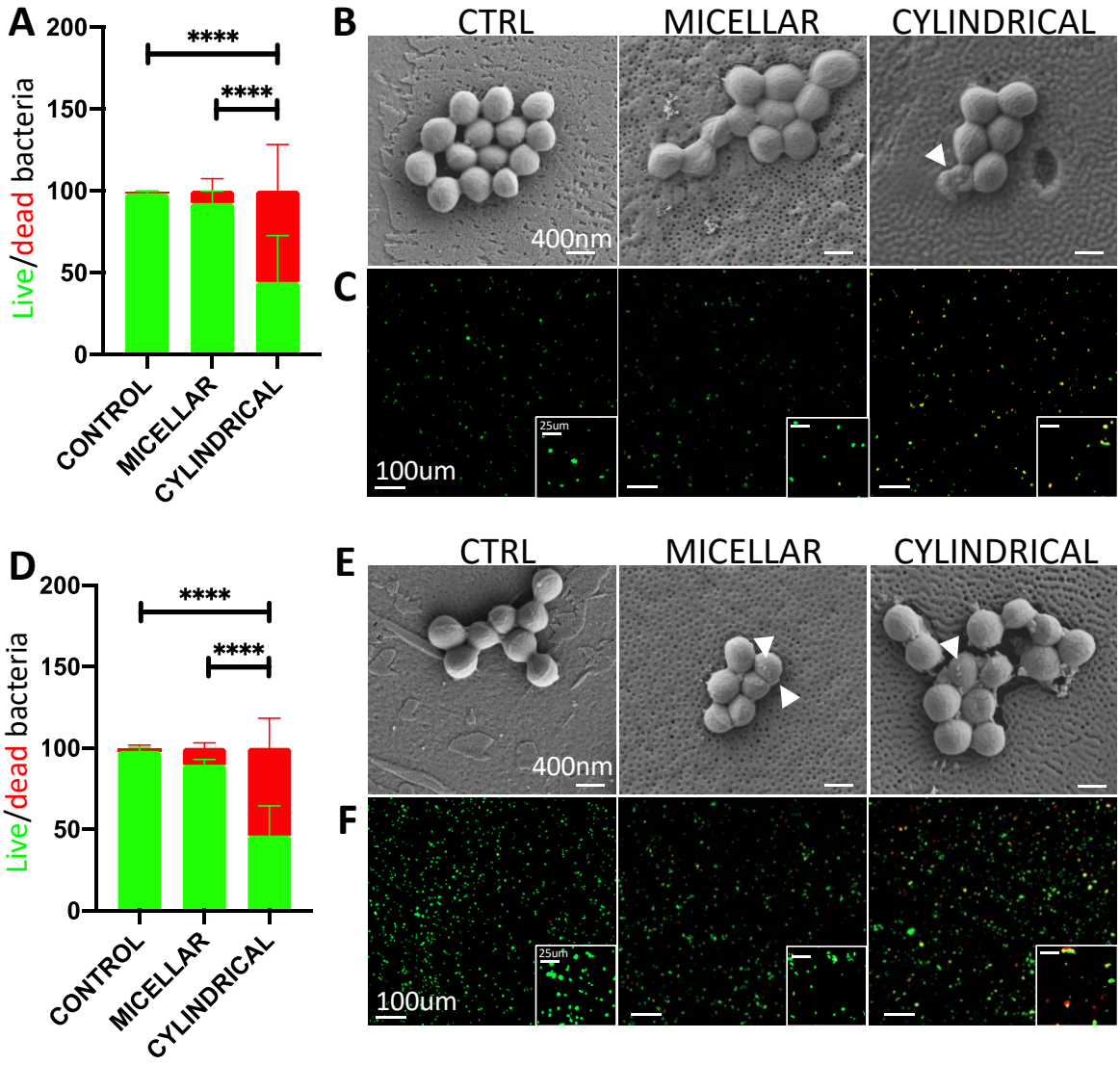

Figure 4. Gram-positive bacteria (*S. aureus*) cultured on bare titanium (control, CTRL) and coated titanium substrates for (A-C) 30 and (D-F) 90 min: (A, D) quantitative data obtained by live/dead assay; (B, E) representative SEM images of *S. aureus* (white arrows show damaged cells); and (C-F) representative fluorescence microscopy images of bacteria on different patterns after live dead assay (live bacteria are stained in green and dead ones in yellow/red). Statistical differences: ****$p < 0.0001$.

View Article Online
DOI: 10.1039/D1TB01352E

The developed patterns have relatively small height; thus, the previously proposed bactericidal mechanism based on the penetration of the nanofeatures in the cell wall[39-42] is not applicable for these coatings as confirmed by the SEM images (Figs. 3E and 4E). The alternative mechanism associated with the fragilization of the bacterial wall during the adhesion process[43] is most probably in play for the herein-developed coatings and in agreement with the observed higher sensitivity of the *E. coli* compared to *S. aureus.* The *E. coli* walls are thinner than the *S. aureus* ones and gram-negative bacteria have a higher lipid content (more hydrophobic) in the cell wall than gram-positive bacteria.[36] Moreover, *E. coli* growth involves an elongation process, which weakens their walls because of the increased mechanical stress during this process.[37] On the other hand, *S. aureus* grows by septum formation – they synthesize cell wall at the septum, i.e. their wall is more resistant during the growth.[38] These strain differences can explain the observed results. Notably, the developed nanopatterns have different surface chemistry – the cylindrical nanopatterns contain hydrophobic PS and hydrophilic P2VP domains, while only PS is exposed on the surface of the micellar structure. The PV2P enables interactions with the hydrophilic portion of the bacterial wall lipopolysaccharides, enhancing the interactions between bacteria and nanopattern and, hence, the bacterial death. The more hydrophobic wall of *E. coli* (Gramm negative) is expected to have increased contact with the micellar pattern than with the Ti alone (used as a control), and indeed, the micellar pattern is enough to reduce considerably the number of viable cells of *E. coli* but not in *S. aureus.*

In addition to the similar behavior observed for the bacteria on nanopatterns either on glass or on Ti,[19] there are differences in the toxicity to *S. aureus*. While the bacterial death was around 20% for cylindrical nanopatterns on glass substrates, it reached about 50% when Ti was used as a substrate. Thus, the nanopatterns present a substantially improved contact-killing effect to *S. aureus* on Ti compared to glass. Given that peri-implantitis is a polymicrobial disease, the observed contact-killing effect over gram-negative and gram-positive bacteria is of great relevance for future applications. Moreover, *S. aureus* has a high affinity to Ti and its hindering under the coating can reduce the risk of peri-implantitis in dental implants.[44]

The observed difference between the glass and Ti substrates can be related to the microscale irregularities on the bare Ti surface (Figures 2-4 and S1). It is well known that bacteria tend to sit over the microscale valleys.[45] These irregularities will increment the

View Article Online
DOI: 10.1039/D2TB01352E

surface tension exerted on the bacterial wall because of the higher interactions. This effect will be added to the surface tension exerted by the nanopattern, maximizing the contact-killing effect. Interestingly, these differences also demonstrate the necessity of testing bactericidal properties of relevant materials before translation to the clinics.

Effect of the coatings on mammalian cell attachment

Upon implantation, host cells compete with bacteria to attach to the device surface, and the result of this competitive process is crucial for implant integration.[46] Gingival fibroblasts are the major cell population in the host gingival tissue, and thus, these cells were studied in contact with the developed coatings.[47] The number of adherent cells tends to be higher for the coated substrates when compared with pristine Ti after 30 min (Fig. 5A) although this difference was not statistically significant. At this time point, the cells had a round shape (Fig. 5B).

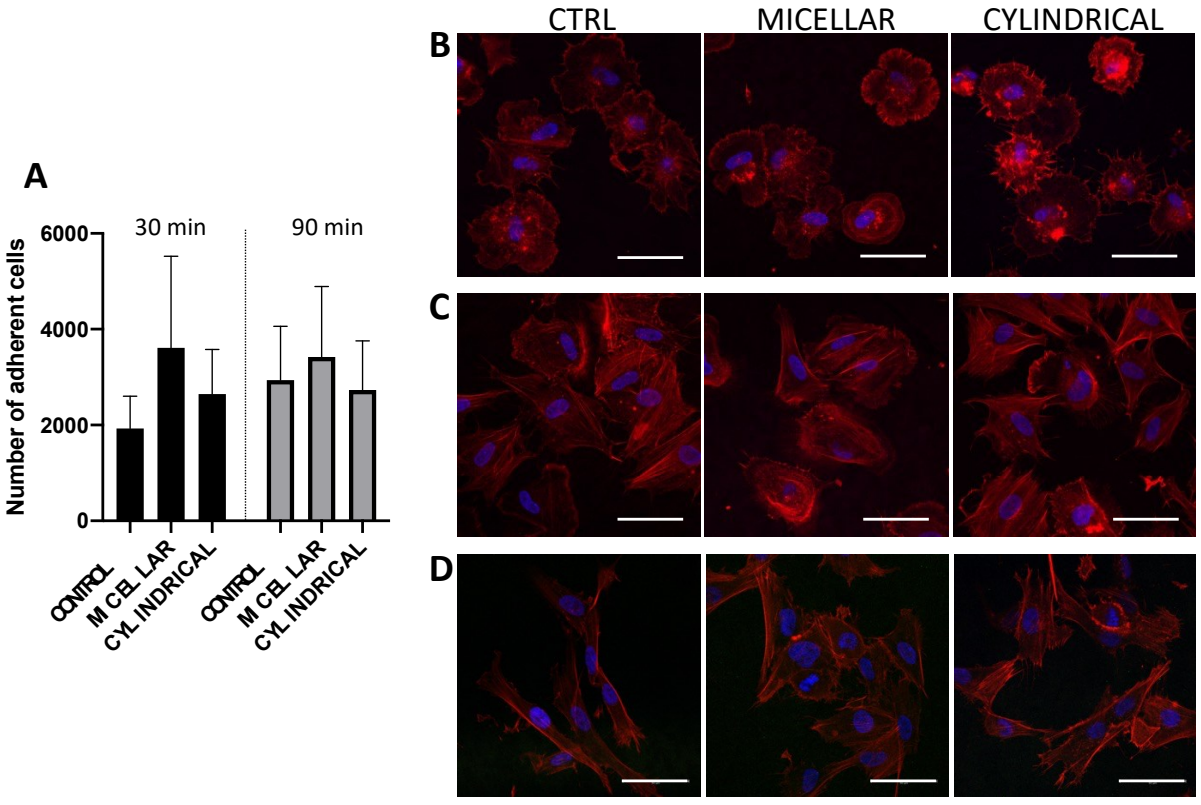

Figure 5. Human gingival fibroblast (HGF) cultured on bare titanium (control, CTRL) and coated substrates for 30 and 90 min: (A) Number of adherent cells for the studied periods; (B, C) Representative fluorescence microscopy images showing cytoskeleton (phalloidin in red) and

View Article Online
DOI: 10.1039/D2TB01352E

nucleus (DAPI in blue) of HGF cultured for (B) 30 min, (C) 90 min and (D) 24 h on the respective substrates. Scale bar is 50 μm.

After 90 min of culture, the number of adherent cells on all substrates was comparable (Fig. 5A), and the morphology was similar – stretched cells acquiring a fibroblastic shape were observed (Fig. 5C). Prolongation of the culture time to 24 h, resulted in further cell elongation and formation of cell clusters (Fig. 5D) that might be beneficial for the implant integration. These results therefore demonstrate that gingival cell attachment on the block copolymer nanopatterns is as good as on Ti - the gold standard for dental implants.

Inflammatory response

The implant placement causes an innate immune response due to the mechanical stress on the host tissue and the unavoidable bacterial and chemical attacks in the oral cavity.[48] In this response, an adequate balance and regulation of pro-inflammatory (M1) and reparative (M2) macrophages along the time is crucial.[49] Thus, we studied macrophage polarization using THP-1 derived macrophages and analyzing specific markers, namely CCR7 for M1 and CD206 for M2, and cell morphology because an elongated shape indicates M2 phenotype.[50] THP-1 derived macrophages cultured on all studied substrates (bare and coated Ti substrates) expressed CCR7 (Fig. 6A,B), showing that the substrates promote M1-like polarization of THP-1 cells. The quantitative data evidenced minor differences between the bare Ti and the patterns (Fig. 6B).

On the other hand, the cells did not express CD206 (Fig. 6C). Still, we observed different cell shapes for the studied substrates (Fig. 6D): cells in contact with the nanopatterns were more elongated compared to cells cultured on bare Ti, and this difference was more pronounced for the cylindrical pattern. Of note, an elongation of the fibroblasts was observed for all substrates (Fig. 5D) and not selectively on the nanopatterns, as is the case in THP-1 cells. Previous studies have shown that macrophages tend to polarize towards M2 phenotype on anisotropic and rough micro- and nanopatterns.[50-52] Nevertheless, we did not observe such a tendency for our nanopatterns: although the micellar nanopattern has higher roughness than the cylindrical one, the macrophages showed a higher aspect ratio on the cylindrical

View Article Online
DOI: 10.1039/D2TB01352E

nanopatterns. The surface chemistry can also influence the phenotypic polarization of macrophages [53]: when hydrophilic and hydrophobic domains are exposed on the surface, we observe more elongated cells, in the case of the cylindrical nanopattern. Altogether these results show that the nanopatterns do not induce strong inflammation maintaining a similar M1/M2 polarization as bare Ti, according to immunostaining results. However, a slight pro-healing M2-like polarization on cylindrical nanopatterns is indicated by the higher aspect ratio of the cells, which in any case might be in early stages given the absence of CD206 staining.

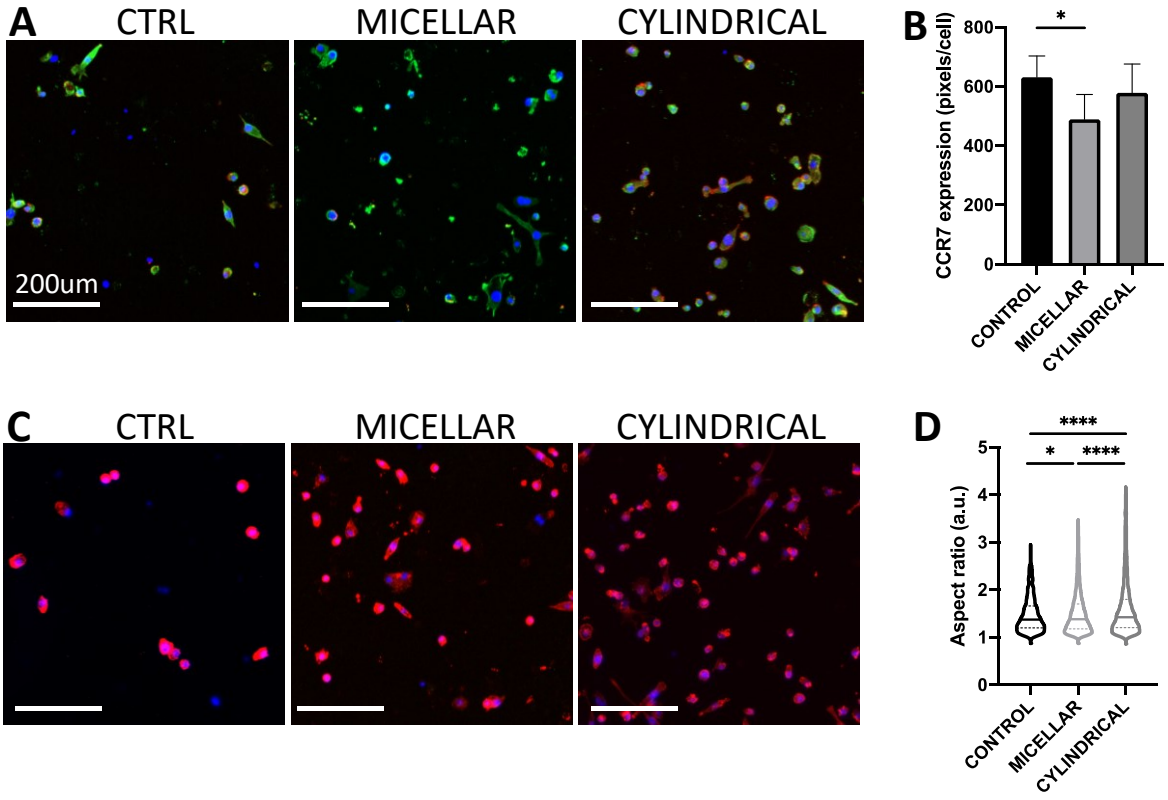

Figure 6. Effect of the nanopatterns on macrophages: (A, C) Representative fluorescence images of the differentiated THP-1 cells in contact with bare Ti (control, CTRL) and the nanopatterns for 24 h (nuclei stained with DAPI in blue and cytoskeleton stained with phalloidin in red). (A) Images showing CCR7 expression (green) and (B) the respective quantification obtained from these images; (C) Cells immunostained for CD206 (green); (D) Effect of the coatings on the THP-1 cells aspect ratio. Continuous thick line represents the median and the doted lines show the higher and the lower quartile. Statistical differences: *p < 0.05, ****p < 0.0001

View Article Online
DOI: 10.1039/D2TB01352E

Conclusions

Block copolymer self-assembly was applied to obtain nanopattern coatings on Ti substrates as a model of a dental implant. The cylindrical nanopatterns presented contact-killing capacity towards *E. coli* and *S. aureus. The surfaces* present similar adhesion and spreading (human gingival fibroblast) and immune response similar (THP-1 cells) to bare Ti. These results suggest the used block copolymers as good candidates for dental Ti implant coating. The following steps should include testing the antibacterial activity in a multispecies biofilm model, examination of mammalian cells proliferation for longer periods and a dynamic co-culture system between mammalian cells and bacteria to simulate as much as possible the dental microenvironment.

Acknowledgments

Portuguese Foundation for Science and Technology for the grants PTDC/QUI-POL/28117/2017, PD/BD/128085/2016 (RF), CEECIND/00814/2017 (RNC) and CEECIND/01375/2017 (MGF).

Bibliography

1. C. N. Elias, D. J. Fernandes, F. M. d. Souza, E. d. S. Monteiro and R. S. d. Biasi, *Journal of Materials Research and Technology*, 2019, **8**, 1060-1069.
2. S. G. Steinemann, *Periodontology 2000*, 1998, **17**, 7-21.
3. A. D. Pye, D. E. Lockhart, M. P. Dawson, C. A. Murray and A. J. Smith, *J Hosp Infect*, 2009, **72**, 104-110.
4. N. A. Valente and S. Andreana, *J Periodontal Implant Sci*, 2016, **46**, 136-151.
5. D. M. Daubert, B. F. Weinstein, S. Bordin, B. G. Leroux and T. F. Flemming, *J Periodontol*, 2015, **86**, 337-347.
6. M. Romandini, C. Lima, I. Pedrinaci, A. Araoz, M. C. Soldini and M. Sanz, *Clin Oral Implants Res*, 2021, **32**, 112-122.
7. T. Q. Guo, K. Gulati, H. Arora, P. P. Han, B. Fournier and S. Ivanovski, *Acta Biomaterialia*, 2021, **124**, 33-49.
8. S. Lavenus, J. C. Ricquier, G. Louarn and P. Layrolle, *Nanomedicine*, 2010, **5**, 937-947.
9. L. Z. Zhao, P. K. Chu, Y. M. Zhang and Z. F. Wu, *Journal of Biomedical Materials Research Part B-Applied Biomaterials*, 2009, **91b**, 470-480.
10. S. Qin, K. H. Xu, B. N. Nie, F. Ji and H. Zhang, *Journal of Biomedical Materials Research Part A*, 2018, **106**, 2531-2539.
11. C. Desrousseaux, V. Sautou, S. Descamps and O. Traore, *Journal of Hospital Infection*, 2013, **85**, 87-93.
12. D. J. Stickler, *Journal of Applied Microbiology*, 2002, **92**, 163s-170s.
13. T. Wei, Q. Yu and H. Chen, *Advanced Healthcare Materials*, 2019, **8**.
14. G. Hazell, L. E. Fisher, W. A. Murray, A. H. Nobbs and B. Su, *J Colloid Interface Sci*, 2018, **528**, 389-399.

View Article Online
DOI: 10.1039/D2TB01352E

15. C. D. Bandara, S. Singh, I. O. Afara, A. Wolff, T. Tesfamichael, K. Ostrikov and A. Oloyede, *ACS Appl Mater Interfaces*, 2017, **9**, 6746-6760.
16. P. Ramburrun, N. A. Pringle, A. Dube, R. Z. Adam, S. D'Souza and M. Aucamp, *Materials (Basel)*, 2021, **14**.
17. Z. Nie and E. Kumacheva, *Nature Materials*, 2008, **7**, 277-290.
18. S. B. Darling, *Progress in Polymer Science*, 2007, **32**, 1152-1204.
19. R. Fontelo, D. Soares da Costa, R. L. Reis, R. Novoa-Carballal and I. Pashkuleva, *Acta Biomater*, 2020, **112**, 174-181.
20. D. V. Nicolau, S. Li, G. Metcalfe, A. Komaromy, R. I. Boysen, D. V. Nicolau and M. T. W. Hearn, presented in part at the Biomedical Applications of Micro- and Nanoengineering IV and Complex Systems, 2008.
21. K. J. Moor, C. O. Osuji and J. H. Kim, *ACS Appl Mater Interfaces*, 2016, **8**, 33583-33591.
22. C. R. Pedrosa, D. Arl, P. Grysan, I. Khan, S. Durrieu, S. Krishnamoorthy and M. C. Durrieu, *Acs Applied Materials & Interfaces*, 2019, **11**, 8858-8866.
23. H. L. Khor, Y. Kuan, H. Kukula, K. Tamada, W. Knoll, M. Moeller and D. W. Hutmacher, *Biomacromolecules*, 2007, **8**, 1530-1540.
24. E. J. Jeong, J. W. Lee, Y. J. Kwark, S. H. Kim and K. Y. Lee, *Colloids and Surfaces B-Biointerfaces*, 2014, **123**, 679-684.
25. S. J. Yeon, J. W. Lee, J. W. Lee, E. J. Jeong, Y. J. Kwark, S. H. Kim and K. Y. Lee, *Soft Matter*, 2012, **8**, 3898-3903.
26. I. Y. Tsai, M. Kimura, R. Stockton, J. A. Green, R. Puig, B. Jacobson and T. P. Russell, *Journal of Biomedical Materials Research Part A*, 2004, **71a**, 462-469.
27. I. A. Monteiro, T. Kollmetz, D. S. Musson, S. R. McGlashan and J. Malmstrom, *Biointerphases*, 2020, **15**.
28. P. A. George, M. R. Doran, T. I. Croll, T. P. Munro and J. J. Cooper-White, *Biomaterials*, 2009, **30**, 4732-4737.
29. J. Y. Cheng, C. A. Ross, E. L. Thomas, H. I. Smith and G. J. Vancso, *Advanced Materials*, 2003, **15**, 1599-+.
30. S. F. Lamolle, M. Monjo, S. P. Lyngstadaas, J. E. Ellingsen and H. J. Haugen, *J Biomed Mater Res A*, 2009, **88**, 581-588.
31. R. Fontelo, D. Soares da Costa, R. L. Reis, R. Novoa-Carballal and I. Pashkuleva, *J Colloid Interface Sci*, 2022, **608**, 1608-1618.
32. N. U. Zitzmann, T. Abrahamsson and J. Lindhe, *Journal of Clinical Periodontology*, 2002, **29**, 456-461.
33. M. Shahabouee, M. Rismanchian, J. Yaghini, A. Babashahi, H. Badrian and H. Goroohi, *Dental Reseach Journal*, 2011, **9**, 215-220.
34. S. M. Stocks, *Cytometry Part A*, 2004, **61a**, 189-195.
35. X. Huang, X. Bao, Y. Liu, Z. Wang and Q. Hu, *Sci Rep*, 2017, **7**, 1860.
36. S. Pogodin, J. Hasan, V. A. Baulin, H. K. Webb, V. K. Truong, T. H. P. Nguyen, V. Boshkovikj, C. J. Fluke, G. S. Watson, J. A. Watson, R. J. Crawford and E. P. Ivanova, *Biophysical Journal*, 2013, **104**, 835-840.
37. A. J. F. Egan, *Molecular Microbiology*, 2018, **107**, 676-687.
38. H. Tzagoloff and R. Novick, *Journal of Bacteriology*, 1977, **129**, 343-350.
39. L. E. Fisher, Y. Yang, M. F. Yuen, W. Zhang, A. H. Nobbs and B. Su, *Biointerphases*, 2016, **11**, 011014.

40. T. Diu, N. Faruqui, T. Sjostrom, B. Lamarre, H. F. Jenkinson, B. Su and M. G. Ryadnov, *Sci Rep*, 2014, **4**, 7122.
41. Y. Yuan and Y. Zhang, *Nanomedicine*, 2017, **13**, 2199-2207.
42. P. M. Tsimbouri, L. Fisher, N. Holloway, T. Sjostrom, A. H. Nobbs, R. M. Meek, B. Su and M. J. Dalby, *Sci Rep*, 2016, **6**, 36857.
43. S. Wu, F. Zuber, K. Maniura-Weber, J. Brugger and Q. Ren, *J Nanobiotechnology*, 2018, **16**, 20.
44. G. R. Persson and S. Renvert, *Clinical Implant Dentistry and Related Research*, 2014, **16**, 783-793.
45. N. Vargas-Alfredo, A. Santos-Coquillat, E. Martinez-Campos, A. Dorronsoro, A. L. Cortajarena, A. del Campo and J. Rodriguez-Hernandez, *Acs Applied Materials & Interfaces*, 2017, **9**, 44270-44280.
46. A. Gristina and H. H. Sherk, *Clinical Orthopaedics and Related Research*, 2004, DOI: 10.1097/01.blo.0000145156.89115.12, 4-12.
47. P. C. Smith, C. Martinez, J. Martinez and C. A. McCulloch, *Frontiers in Physiology*, 2019, **10**.
48. J. Derks and C. Tomasi, *Journal of Clinical Periodontology*, 2015, **42**, S158-S171.
49. H. J. Busscher, H. C. van der Mei, G. Subbiahdoss, P. C. Jutte, J. J. A. M. van den Dungen, S. A. J. Zaat, M. J. Schultz and D. W. Grainger, *Science Translational Medicine*, 2012, **4**.
50. F. Y. McWhorter, T. T. Wang, P. Nguyen, T. Chung and W. F. Liu, *Proceedings of the National Academy of Sciences of the United States of America*, 2013, **110**, 17253-17258.
51. K. M. Hotchkiss, G. B. Reddy, S. L. Hyzy, Z. Schwartz, B. D. Boyan and R. Olivares-Navarrete, *Acta Biomaterialia*, 2016, **31**, 425-434.
52. T. Schmitz, M. Jannasch, T. Weigel, C. Moseke, U. Gbureck, J. Groll, H. Walles and J. Hansmann, *Materials (Basel)*, 2020, **13**.
53. H. M. Rostam, S. Singh, F. Salazar, P. Magennis, A. Hook, T. Singh, N. E. Vrana, M. R. Alexander and A. M. Ghaemmaghami, *Immunobiology*, 2016, **221**, 1237-1246.